CHIN. PHYS. LETT. Vol. 35, No. 11 (2018) 117101

Magnetotransport Properties of a Nodal Line Semimetal TiSi *

Moran Gao(高默然)[1,2], Junbao He(何俊宝)[3], Wenliang Zhu(朱文亮)[1,2], Shuai Zhang(张帅)[1], Xinmin Wang(王欣敏)[1,2], Jing Li(李婧)[1,2], Chaoyang Ma(麻朝阳)[1], Hui Liang(梁慧)[1,2], Zhian Ren(任治安)[1,4], Genfu Chen(陈根富)[1,2,4]**

[1]*Institute of Physics and Beijing National Laboratory for Condensed Matter Physics, Chinese Academy of Sciences, Beijing 100190*

[2]*School of Physical Sciences, University of Chinese Academy of Sciences, Beijing 100049*

[3]*College of Physics and Electronic Engineering, Nanyang Normal University, Nanyang 473061*

[4]*Collaborative Innovation Center of Quantum Matter, Beijing 100190*

(Received 26 September 2018)

We report the magnetoresistance (MR), de Haas-van Alphen (dHvA) effect and Hall effect measurements on a single crystal of TiSi, which is predicted to be a nodal line semimetal. With application of a magnetic field, a metal-to-insulator-like transition in $\rho(T)$ and a nonsaturating MR are observed at low temperatures. The dHvA oscillations reveal a small Fermi-surface pocket with a nontrivial Berry phase. The analysis of the nonlinear Hall resistivity shows that TiSi is a multiband system with low carrier densities and high mobilities. All these results unambiguously prove the existence of Dirac fermions in TiSi.

PACS: 71.55.Ak, 71.30.+h, 75.47.−m, 81.10.Fq DOI: 10.1088/0256-307X/35/11/117101

The discovery of topological semimetals (TSMs) has aroused intensive interest in condensed physics and material science. Due to the special band structure, these materials possess exotic physical properties and potential applications in the future.[1−3] According to the nodal points distribution in momentum and the degeneracy of the crossed band, the TSMs can be classified into three categories: Dirac semimetals (DSMs),[4−10] Weyl semimetals (WSMs)[11−18] and nodal line semimetals (NLSMs).[19−24] WSMs have Weyl points, which come from two non-degeneracy bands crossing, while for the DSMs, the crossing of two double-degeneracy bands near the Fermi level generates a fourfold degenerate nodal point, which is protected by time-reversal symmetry and inversion symmetry. When one of the symmetries is destroyed, WSMs will be generated. Very recently, topological semimetals with triply degenerate nodal points were explored in WC-type compounds.[25−29] An unconventional feature for such a system is that the splitting of triply-degenerate nodes into pairs of Weyl nodes is direction dependent.[25]

Unlike DSMs and WSMs, NLSMs show a closed ring or a continuous line formed by nodal points near the Fermi level and have nearly flat surface states.[23,24] The unique electronic structure could lead to giant surface Freidel oscillations, long-range Coulomb interactions,[20,30] and other amazing properties. However, only a few materials were investigated as NLSMs, such as $PbTaSe_2$, ZrSiS, Be and $PtSn_4$.[20,31−33] Recently, TiSi was predicted to be a new NLSM and the nodal ring lies on $k_y = 0$ plane. The high energy nodal point is located at 0.1 eV above the Fermi level, the low energy nodal point is located at 0.18 eV below the Fermi level, and the nodal ring is very close to the Fermi surface.[34] Thus it provides a perfect platform to explore the exotic electronic properties in NLSMs.

In this work, we successfully grow the single crystals of TiSi and studied its physical properties. We find that TiSi has a magnetic field induced metal-to-insulator-like transition and a positive nonsaturating MR. Hall resistivity measurement indicates that TiSi is a multiband system, and the main carriers are electron type with low carrier density and high mobility. The analysis of dHvA oscillations shows that TiSi has a small cross-sectional area of Fermi surface and light cyclotron effective mass. The detection of a nontrivial π Berry phase provides strong evidence for the existence of Dirac fermions in TiSi.

Single crystals of TiSi were grown from Zn-flux. The arc melted TiSi with moderate Zn were sealed in an evacuated quartz tube. The quartz tube was heated to 1150℃, held for 30 h, and then cooled slowly to 700℃, where the plentiful Zn was decanted using a centrifuge. The residual Zn-flux was removed by hydrochloric acid at 80℃. The obtained single crystals are rod-like with lengths of around 1 mm as shown in the right inset of Fig. 1(b). The single crystals were characterized by x-ray diffraction (XRD) on a PANalytical diffractometer with Cu K_α radiation at room temperature. The crystallization directions were identified by the Laue diffraction. The element compositions were confirmed by Oxford X-Max energy disper-

*Supported by the National Key Research Program of China under Grant Nos 2016YFA0401000 and 2016YFA0300604, the National Basic Research Program of China under Grant No 2015CB921303, the Strategic Priority Research Program (B) of Chinese Academy of Sciences under Grant No XDB07020100, and the National Natural Science Foundation of China under Grant No 11874417.

**Corresponding author. Email: gfchen@iphy.ac.cn

© 2018 Chinese Physical Society and IOP Publishing Ltd

sive x-ray (EDX) spectroscopy analysis on a Hitachi S-4800 scanning electron microscope. The electrical transport and magnetic characters were measured using a Quantum Design PPMS-9T and an MPMS-7T SQUID VSM system, respectively.

The powder XRD pattern of TiSi obtained by grinding numerous single crystals is shown in Fig. 1(a). The powder diffraction peaks indicate that the crystal structure of TiSi is the orthorhombic lattice with space group $Pnma$ (No.62). The refined lattice parameters $a = 6.541(1)$ Å, $b = 3.641(3)$ Å and $c = 5.003(3)$ Å are in agreement with the reported values.[34,35] The absence of any other reflections indicates that no foreign phases or residuals of flux are present in the single crystals. Figure 1(b) shows the XRD pattern recorded for a typical TiSi single crystal, in which all peaks match with the (011) reflections. The Laue diffraction of TiSi single crystal indicates that the crystal grows preferentially along a-axis. EDX spectroscopy analysis reveals that the atomic composition of the crystals is Ti:Si=1:1 with the accuracy of EDX. No obvious Zn impurity was detected.

Figure 2 shows the electrical transport properties of TiSi. The temperature dependence of the resistivity under selected magnetic fields with $B \perp (011)$ plane and $I \parallel a$-axis is presented in Fig. 2(a). In zero field, the resistivity shows metallic behavior and the residual resistivity ratio [RRR=$\rho(300\,\mathrm{K})/\rho(2\,\mathrm{K})$] is around 15, which is smaller than that of other TSMs.[25,32,36] With increasing the magnetic field, the resistivity ρ increases gradually and shows a clear upturn at low temperatures. Similar to other TSMs, ρ saturates at very low temperatures, and results in a resistivity plateau.[11,12,25,32,36]

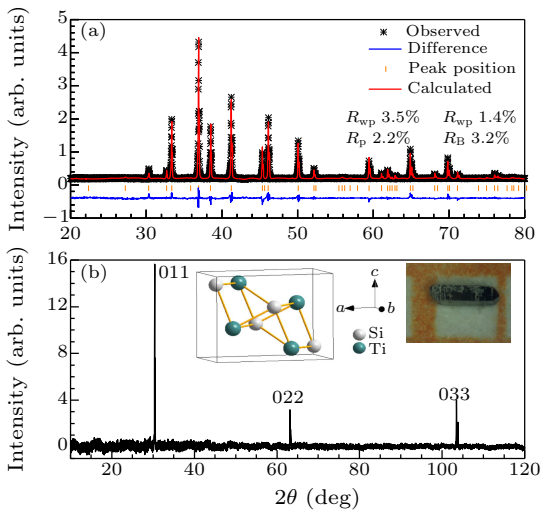

Fig. 1. (Color online) (a) Power XRD pattern of TiSi obtained by grinding numerous single crystals and the refinement results. (b) The single crystal XRD pattern of TiSi. The left inset shows the crystal structure of TiSi. The right inset displays the optical image of a TiSi single crystal sample.

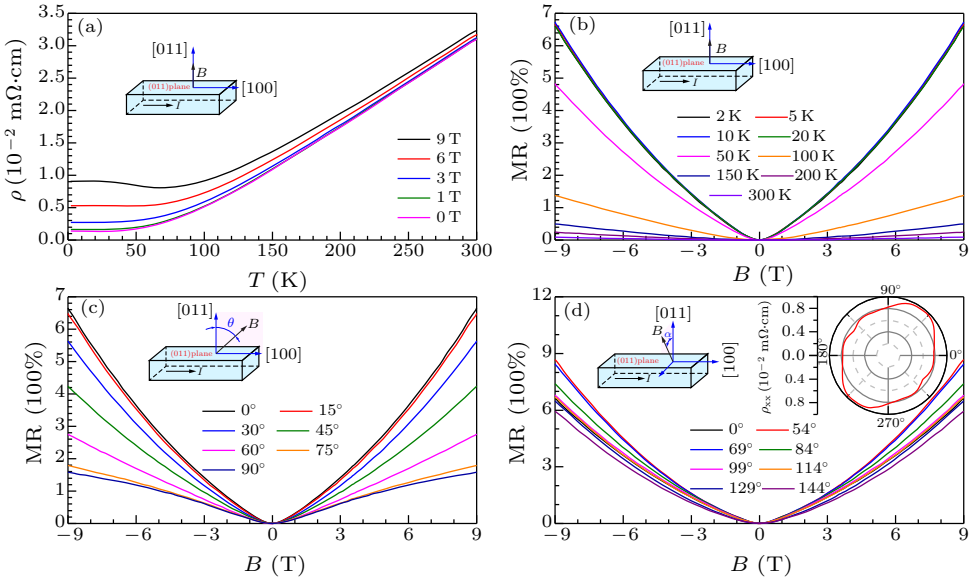

Fig. 2. (Color online) Transport properties of TiSi. (a) Temperature dependence of the resistivity ρ under magnetic fields with $B \perp (011)$ plane and $I \parallel a$-axis. The inset displays the measurement configuration. (b) Magnetic field dependence of MR at various temperatures with $B \perp (011)$ plane and $I \parallel a$-axis. (c) Magnetic field dependence of MR at 2 K with the magnetic field rotated from $B \perp (011)$ plane ($\theta = 0°$) to $B \parallel a$-axis ($\theta = 90°$). The inset shows the measurement configuration. (d) Magnetic field dependence of MR at 2 K with the magnetic field rotated in the bc-plane. The left inset reveals the measurement configuration. The right inset presents a polar plot of the angular dependence of the MR as the magnetic field is rotated in the bc-plane at 2 K and 9 T.

Figure 2(b) presents the magnetic field dependence of MR at various temperatures for $B \perp (011)$ plane and $I \parallel a$-axis. The MR displays no apparent change at temperature lower than 20 K and then decreases gradually with increasing temperature. The magnetic field dependence of MR at 2 K with magnetic field rotated from $B \perp (011)$ plane to $B \parallel a$-axis is shown in Fig. 2(c). The MR decreases gradually from $B \perp (011)$ plane ($\theta = 0°$) to $B \parallel I$ ($\theta = 90°$). The maximum value of MR is about 650% and the minimum value

of MR is below 200%. No negative magnetoresistance was observed for $B \parallel I$. Figure 2(d) shows the magnetic field dependence of MR at 2 K with the magnetic field rotated in the *bc*-plane. The MR increases gradually with increasing α and reaches a maximum at $\alpha = 54°$ where $B \parallel b$-axis. From $\alpha = 54°$ to $\alpha = 144°$, the MR decreases monotonically, and the value of $\mathrm{MR_{max}}/\mathrm{MR_{min}}$ is about 1.5, which is very small compared with other TSMs.[11,12,25,36,37] The MR displays a nearly quadratic field dependence as the magnetic field close to 0 T and has no tendency of saturation up to 9 T. The right inset shows a polar plot of the angular dependence of the MR at 2 K and 9 T as the magnetic field is rotated in the *bc*-plane. It indicates that the MR has a small anisotropy in the *bc*-plane, which is very different from the butterfly shaped MR observed in ZrSiS,[37] in which the electric current flows through the plane where the nodal line lies while it is not in our case.

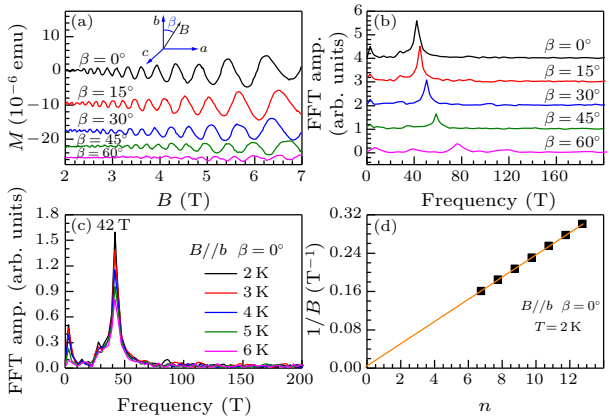

Fig. 3. (Color online) (a) Magnetization M versus magnetic field B with the magnetic field rotated in the *ab*-plane at 2 K, and the inset shows the measurement configuration. (b) Angular dependence of the FFT spectra of the dHvA oscillations at 2 K by rotating the magnetic field in the *ab*-plane. (c) The FFT spectra of the dHvA oscillations at various temperatures for $B \parallel b$-axis. (d) Landau-level index plots $1/B$ versus $n - 1/4$ for $B \parallel b$-axis at 2 K.

The dHvA effect is a very powerful tool in the studies of Fermi surface (FS) of materials. Figure 3(a) presents the isothermal magnetization of a single crystal at 2 K with the magnetic field rotated in the *ab*-plane. To make $B \parallel b$-axis, the sample is rotated by an angle of α ($\approx 54°$), which is determined by the maximum of the MR as the magnetic field rotated in the *bc*-plane. We find that the dHvA amplitudes become weaker and finally disappear when the magnetic field is tilted up to 60° from the normal to (010) plane. The corresponding fast Fourier transform (FFT) spectra of the dHvA oscillations is shown in Fig. 3(b). For $B \perp (010)$ plane, only one fundamental frequency at about $F = 42$ T can be seen. The frequency shifts to higher value as the magnetic field is tilted, which is consistent with the theoretical calculation:[34] the Dirac nodal ring is located in the $k_y = 0$ plane. Using the Onsager relation $F = (\Phi_0/2\pi^2)A_\mathrm{F}$, where F is the FFT frequency, Φ_0 is the flux quantum, the cross-sectional area of FS, A_F, could be obtained. For $F = 42$ T, A_F is roughly estimated to be 0.40 nm^{-2}, only occupying 0.33% of the first Brillouin zone (BZ). The FFT amplitude of dHvA oscillations at selected temperatures is shown in Fig. 3(c). The amplitude drops dramatically with increasing the temperature. The temperature dependence of the amplitude can be fitted with the Lifshitz–Kosevitch formula[38]

$$\text{amplitude} \propto \frac{2\pi^2 k_\mathrm{B} T m^*/\hbar e B}{\sinh(2\pi^2 k_\mathrm{B} T m^*/\hbar e B)}, \tag{1}$$

where k_B is the Boltzmann constant, m^* is the cyclotron effective mass, $\hbar$ is Planck's constant divided by 2π, and e is the bare electron charge. The obtained cyclotron effective mass is very small, $m^* = 0.08 m_\mathrm{e}$ with m_e being the bare electronic mass. The small cross-sectional area of FS and the light cyclotron effective mass are the typical features of the topological semimetals, which have been observed in other TSMs such as Ta_3S_2, WC, TaAs and ZrTe.[11,12,25,26]

The value of the Berry phase (φ_B) is usually used to judge the topological property of a material. Here we also analyze the topological property of TiSi using the Onsager phase factor $\gamma = 1/2 - (\varphi_\mathrm{B}/2\pi)$, which is 0 or 1 for the nontrivial φ_B and 1/2 for the trivial φ_B. The value of γ is estimated by the relationship between the peak position of oscillations ($1/B$) and Landau index of $n - 1/4$ as shown in Fig. 3(d). The linear extrapolation of the Landau level index $n - 1/4$ versus $1/B$ plot gets the value of $\gamma - \delta$ (δ is a phase offset and the value of δ is $\pm 1/8$ for three-dimensional system and 0 for two-dimensional system). We find that the obtained value is around -0.12 indicating the presence of nontrivial π Berry phase.[39–41]

To further study the transport properties of this material, the magnetic field dependence of Hall resistivity was also measured. As shown in Fig. 4(a), ρ_{xy} presents a nonlinear characteristic indicating that TiSi belongs to a multiband system and the negative slope suggests that the electron-type carriers dominate the transport process. We analyse the Hall data by fitting the Hall conductivity σ_{xy} using the semiclassical two-band model[42,43]

$$\sigma_{xy} = \frac{\rho_{xy}}{\rho_{xx}^2 + \rho_{xy}^2} = \left[\frac{n_1\mu_1^2}{1 + (\mu_1 B)^2} + \frac{n_2\mu_2^2}{1 + (\mu_2 B)^2}\right] eB, \tag{2}$$

where n_1 (or n_2) denotes the carrier density and μ_1 (or μ_2) represents the mobility of carriers, respectively. The Hall conductivity σ_{xy} can be fitted well by the two-band model as the temperature below 200 K. The inset of Fig. 4(a) shows the best fitting curve for $T = 2$ K, which brings out two channels of electron-type carriers with $n_1 = 1.4 \times 10^{20}\,\mathrm{cm}^{-3}$, $n_2 = 2.0 \times 10^{17}\,\mathrm{cm}^{-3}$, $\mu_1 = 4.9 \times 10^3\,\mathrm{cm}^2\mathrm{V}^{-1}\mathrm{s}^{-1}$, and $\mu_2 = 4.0 \times 10^4\,\mathrm{cm}^2\mathrm{V}^{-1}\mathrm{s}^{-1}$. Figures 4(b) and 4(c) display the temperature dependence of the mobilities and densities of the two kinds of electrons, where n_1

is over one order of magnitude larger than that of n_2 at low temperatures, and both n_1 and n_2 tend to decrease simultaneously with the decrease of the temperature above 50 K. However, μ_1 is almost independent of temperature, while μ_2 dramatically increases with decreasing temperature. At high temperatures, the mobilities of the two kinds of electrons tend to the same value. In this case, the nonsaturating MR of TiSi cannot be derived from the compensation mechanism of carriers, which is the main reason for the large nonsaturating MR observed in other TSMs.[12,25]

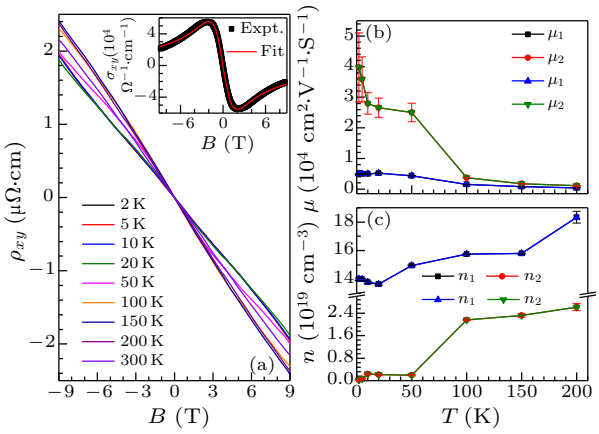

Fig. 4. (Color online) (a) The magnetic field dependence of Hall resistivity ρ_{xy} at various temperatures. The inset presents the experimental data of Hall conductivity and the fitted curve at 2 K. (b) The temperature dependence of carrier mobilities. (c) The temperature dependence of carrier densities.

In conclusion, we have successfully grown the single crystal of TiSi, which is predicted to be a nodal line semimetal. The temperature-dependent resistivity measurement shows a metallic behavior at zero field and a magnetic-field-induced metal-to-insulator-like transition. The analysis of the dHvA oscillations indicates that TiSi has a simple FS with small cross-sectional area of FS and light cyclotron effective mass. Hall resistivity measurement reveals that TiSi is a multiband system and has low carrier densities and high mobilities. The observation of the nontrivial π Berry phase strongly indicates the existence of Dirac fermions. We hope this work can provide valuable clues for further research on TiSi and other NLSMs.

References

[1] Weng H M et al 2016 *J. Phys.: Condens. Matter* **28** 303001
[2] Bansil A et al 2016 *Rev. Mod. Phys.* **88** 021004
[3] Chiu C K et al 2016 *Rev. Mod. Phys.* **88** 035005
[4] Wang Z J et al 2012 *Phys. Rev.* B **85** 195320
[5] Neupane M et al 2014 *Nat. Commun.* **5**
[6] Young S M et al 2012 *Phys. Rev. Lett.* **108** 140405
[7] Liang T et al 2015 *Nat. Mater.* **14** 280
[8] Liu Z K et al 2014 *Nat. Mater.* **13** 677
[9] Wang Z J et al 2013 *Phys. Rev.* B **88** 125427
[10] Liu Z K et al 2014 *Science* **343** 864
[11] Chen D et al 2016 *Phys. Rev.* B **94** 174411
[12] Huang X C et al 2015 *Phys. Rev.* X **5** 031023
[13] Xu S Y et al 2015 *Science* **349** 613
[14] Liu Z K et al 2016 *Nat. Mater.* **15** 27
[15] Weng H M, Fang C, Fang Z, Bernevig B A and Dai X 2015 *Phys. Rev.* X **5** 011029
[16] Lv B Q, Weng H M, Fu B B, Wang X P, Miao H, Ma J, Richard P, Huang X C, Zhao L X, Chen G F, Fang Z, Dai X, Qian T and Ding H 2015 *Phys. Rev.* X **5** 031013
[17] Huang S M, Xu S Y, Belopolski I, Lee C C, Chang G Q, Wang B K, Alidoust N, Bian G, Neupane M, Zhang C L, Jia S, Bansil A, Lin H and Hasan M Z 2015 *Nat. Commun.* **6**
[18] Soluyanov A A, Gresch D, Wang Z J, Wu Q S, Troyer M, Dai X and Bernevig B A 2015 *Nature* **527** 495
[19] Xie L S, Schoop L M, Seibel E M, Gibson Q D, Xie W W and Cava R J 2015 *APL Mater.* **3** 083602
[20] Li R H, Ma H, Cheng X Y, Wang S L, Li D Z, Zhang Z Y, Li Y Y and Chen X Q 2016 *Phys. Rev. Lett.* **117** 096401
[21] Heikkila T T and Volovik G E 2011 *JETP Lett.* **93** 59
[22] Weng H M, Liang Y Y, Xu Q N, Yu R, Fang Z, Dai X and Kawazoe Y 2015 *Phys. Rev.* B **92** 045108
[23] Fang C, Weng H M, Dai X and Fang Z 2016 *Chin. Phys.* B **25** 117106
[24] Burkov A A, Hook M D and Balents L 2011 *Phys. Rev.* B **84** 235126
[25] He J B, Chen D, Zhu W L, Zhang S, Zhao L X, Ren Z A and Chen G F 2017 *Phys. Rev.* B **95** 195165
[26] Zhu W L, He J B, Zhang S, Chen D, Shan L, Ren Z A and Chen G F 2017 arXiv:1707.00942
[27] Bradlyn B, Cano J, Wang Z J, Vergniory M G, Felser C, Cava R J and Bernevig B A 2016 *Science* **353** aaf5037
[28] Weng H M, Fang C, Fang Z and Dai X 2016 *Phys. Rev.* B **94** 165201
[29] Zhu Z M, Winkler G W, Wu Q S, Li J and Soluyanov A A 2016 *Phys. Rev.* X **6** 031003
[30] Huh Y, Moon E G and Kim Y B 2016 *Phys. Rev.* B **93** 035138
[31] Bian G, Chang T R, Sankar R, Xu S Y, Zheng H, Neupert T, Chiu C K, Huang S M, Chang G Q, Belopolski I, Sanchez D S, Neupane M, Alidoust N, Liu C, Wang B K, Lee C C, Jeng H T, Zhang C L, Yuan Z J, Jia S, Bansil A, Chou F C, Lin H and Hasan M Z 2016 *Nat. Commun.* **7** 10556
[32] Mun E, Ko H, Miller G J, Samolyuk G D, Bud'ko S L and Canfield P C 2012 *Phys. Rev.* B **85** 035135
[33] Neupane M, Belopolski I, Hosen M M, Sanchez D S, Sankar R, Szlawska M, Xu S Y, Dimitri K, Dhakal N, Maldonado P, Oppeneer P M, Kaczorowski D, Chou F C, Hasan M Z and Durakiewicz T 2016 *Phys. Rev.* B **93** 201104
[34] Li J X, Ma H, Xie Q, Feng S B, Ullah S, Li R H, Dong J H, Li D Z, Li Y Y and Chen X Q 2018 *Sci. Chin. Mater.* **61** 23
[35] Agarwal S, Cotts E J, Zarembo S, Kematick R and Myers C 2001 *J. Alloys Compd.* **314** 99
[36] Ali M N, Xiong J, Flynn S, Tao J, Gibson Q D, Schoop L M, Liang T, Haldolaarachchige N, Hirschberger M, Ong N P and Cava R J 2014 *Nature* **514**
[37] Wang X F, Pan X C, Gao M, Yu J H, Jiang J, Zhang J R, Zuo H K, Zhang M H, Wei Z X, Niu W, Xia Z C, Wan X G, Chen Y L, Song F Q, Xu Y B, Wang B G, Wang G H and Zhang R 2016 *Adv. Electron. Mater.* **2** 1600228
[38] Shoenberg D 1984 *Magnetic Oscillations in Metals* (Cambridge: Cambridge University)
[39] Murakawa H, Bahramy M S, Tokunaga M, Kohama Y, Bell C, Kaneko Y, Nagaosa N, Hwang H Y and Tokura Y 2013 *Science* **342** 1490
[40] Mikitik G P and Sharlai Y V 1999 *Phys. Rev. Lett.* **82** 2147
[41] He J B, Fu Y, Zhao L X, Liang H, Chen D, Leng Y M, Wang X M, Li J, Zhang S, Xue M Q, Li C H, Zhang P, Ren Z A and Chen G F 2017 *Phys. Rev.* B **95** 045128
[42] Ashcraft N W and Mermin N D 1976 *Solid Sate Physics* (New York: Holt, Rinehart and Winston)
[43] Hurd C M 1972 *The Hall Effect in Metals and Alloys* (Cambridge: Cambridge University)